A-type antiferromagnetic order in the Zintl-phase insulator $EuZn_2P_2$

Tanya Berry,[1,2,*] Veronica J. Stewart,[1,2] Benjamin W. Y. Redemann,[1,2] Chris Lygouras,[2] Nicodemos Varnava,[3] David Vanderbilt,[3] and Tyrel M. McQueen[1,2,4,†]

[1]*Department of Chemistry, Johns Hopkins University, Baltimore, Maryland 21218, USA*
[2]*Institute for Quantum Matter, William H. Miller III Department of Physics and Astronomy, Johns Hopkins University, Baltimore, Maryland 21218, USA*
[3]*Department of Physics & Astronomy, Rutgers University, Piscataway, New Jersey 08854, USA*
[4]*Department of Materials Science and Engineering, Johns Hopkins University, Baltimore, Maryland 21218, USA*

(Received 2 April 2022; revised 28 July 2022; accepted 29 July 2022; published 17 August 2022)

Zintl phases, containing strongly covalently bonded frameworks with separate ionically bonded ions, have emerged as a critical materials family in which to couple magnetism and strong spin-orbit coupling to drive diverse topological phases of matter. Here we report the single-crystal synthesis, magnetic, thermodynamic, transport, and theoretical properties of the Zintl compound $EuZn_2P_2$ that crystallizes in the anti-La_2O_3 ($CaAl_2Si_2$) $P\text{-}3m1$ structure, containing triangular layers of Eu^{2+} ions. In-plane resistivity measurements reveal insulating behavior with an estimated activation energy of $E_g = 0.11$ eV. Specific heat and magnetization measurements indicate antiferromagnetic ordering at $T_N = 23$ K. Curie-Weiss analysis of in-plane and out of plane magnetic susceptibility from $T = 150$ to 300 K yields $p_{\text{eff}} = 8.61$ for $\mu_0 H \perp c$ and $p_{\text{eff}} = 7.74$ for $\mu_0 H // c$, close to the expected values for the $4f^7$ $J = S = 7/2$ Eu^{2+} ion and indicative of weak anisotropy. Below T_N, a significant anisotropy of $\chi_\perp/\chi_{//} \approx 2.3$ develops, consistent with *A*-type magnetic order as observed in isostructural analogs and as predicted by the density functional theory calculations reported herein. The positive Weiss temperatures of $\theta_W = 19.2$ K for $\mu_0 H \perp c$ and $\theta_W = 41.9$ K for $\mu_0 H // c$ show a similar anisotropy and suggest competing ferromagnetic and antiferromagnetic interactions. Comparing Eu magnetic ordering temperatures across trigonal EuM_2X_2 (M = divalent metal, X = pnictide) shows that $EuZn_2P_2$ exhibits the highest ordering temperature, with variations in T_N correlating with changes in expected dipolar interaction strengths within and between layers and independent of the magnitude of electrical conductivity. These results provide experimental validation of the crystochemical intuition that the cation Eu^{2+} layers and the anionic $(M_2X_2)^{2-}$ framework can be treated as electronically distinct subunits, enabling further predictive materials design.

DOI: 10.1103/PhysRevB.106.054420

I. INTRODUCTION

Zintl-phase materials are known to exhibit various phenomena including topological insulators, Dirac semimetals, colossal magnetoresistance, anomalous Hall effect, and spin Hall effect, with applications ranging from thermoelectricity, superconductivity, catalysis, spintronics, and optoelectronics, to solar cells [1–15]. Zintl phases typically consist of a strongly covalently bonded anionic framework with separate cations to provide charge balance. Due to this difference in bonding types, the cationic and anionic subunits can often be tuned or modified independently, enabling systematic materials design of phenomena that requires precise tuning of multiple factors simultaneously [14]. A recent example of the success of this tunability is the discovery of magnetic topological insulators in $EuIn_2As_2$ and $MnBi_2Te_4$, where the electronic structure of the anionic framework provides the topology, while the magnetic order comes from distinct electrons on the cations [1,6,16].

When the cationic framework is constructed of magnetic ions and the anionic framework is nonmagnetic with a closed-shell electron configuration, Zintl phases can realize a variety of magnetic lattices and enable concrete comparisons to analytical theories [17,18]. Further, adjusting the electronic structure of the anionic framework with a fixed cationic lattice enables determination of the key interaction pathways within and between structural subunits, critical knowledge needed to discover and engineer novel electronic and magnetic phases.

More concretely, layered, insulating, Eu-based EuM_2X_2 (M = metal, X = pnictide) Zintl compounds provide realizations of weakly coupled square or triangular magnetic lattices, depending on the preferred geometry of the M_2X_2 layer ($ThCr_2Si_2$-type or anti-La_2O_3-type, respectively). The half-filled, $L = 0$ nature of Eu^{2+} ($J = S = 7/2$) ensures minimal effects from local crystal fields (single-ion anisotropy). In such materials, Eu can be partially or fully substituted with Ba, Sr, and/or Ca to dilute the magnetic lattice while holding the overall unit cell parameters constant. Alternatively, the anionic framework can be adjusted to change the cation ion separation and hence strength of the magnetic interactions within or between cationic layers. By adjusting the electronic structure of the anionic framework, the degree of interaction

*tberry@ucdavis.edu
†mcqueen@jhu.edu

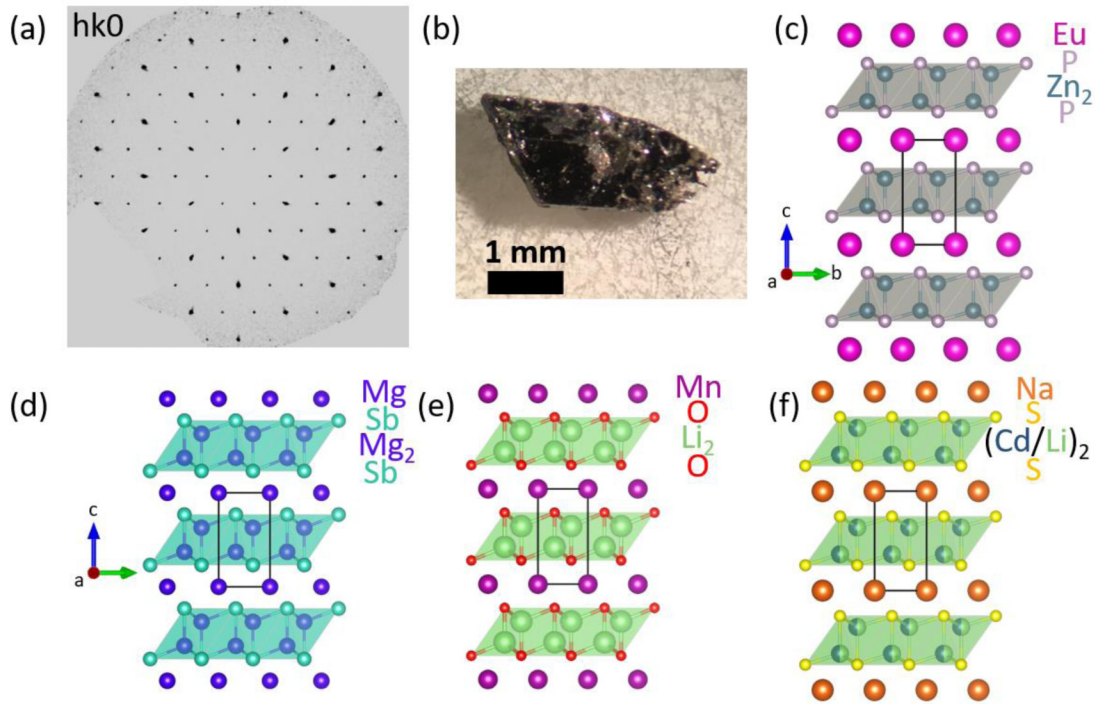

FIG. 1. (a) Single-crystal precession image of the (*hk*0) plane. (b) As-grown single crystal of $EuZn_2P_2$. Structures of (c) $EuZn_2P_2$, (d) Mg_3Sb_2, (e) Li_2MnO_2, and (f) $NaLiCdS_2$ that crystallize in *P*-3*m*1 (164) and are anti-La_2O_3 ($CaAl_2Si_2$) structures containing 2D trigonal layers of cations separated by anionic layers of edge-sharing tetrahedra. The black box represents the unit cell in each case [27–31].

screening (or enhancement due to, e.g., superexchange or RKKY interactions) is also variable.

In this work, we report the physical properties of $EuZn_2P_2$ single crystals prepared via flux growth, and provide comparisons to other members of the family. Single-crystal x-ray diffraction at $T = 213$ K confirms the previously reported $CaAl_2Si_2$ structure type, with triangular Eu^{2+} layers separated by $(Zn_2P_2)^{2-}$ layers of edge-sharing tetrahedral [18]. Bulk resistivity measurements reveal insulating behavior with an estimated activation energy of $E_g = 0.11$ eV. Specific heat measurements reveal a lambda anomaly at $T_N = 23$ K, with a broad hump continuing down to $T = 2$ K. After fitting a phonon model to $T > 25$ K, the estimated integrated change in recovered magnetic entropy is $\Delta S_{\text{mag}} = 11.3\,\text{J mol}^{-1}\,\text{K}^{-1}$ from $T = 0$ K to $\text{T} = \text{T}_\text{N}$, close to $\frac{2}{3}$ of the total entropy recovered for $S = 7/2$ ions, $\Delta S_{\text{mag}} = R\ln(8)$. Magnetization measurements show a cusp at $T_N = 23$ K, indicative of the formation of Eu antiferromagnetic order. Above T_N, Curie-Weiss analysis yields $p_{\text{eff}} = 8.61$ for $\mu_0 H \perp c$ and $p_{\text{eff}} = 7.74$ for $\mu_0 H // c$, close to the expected value for $4f^7$ $J = S = 7/2$ Eu^{2+} ions ($p_{\text{eff}} = 7.94$). Below T_N, a significant anisotropy of $\chi_\perp/\chi_{//} \approx 2.3$ develops, consistent with *A*-type magnetic order as observed in isostructural analogs. The positive Weiss temperatures of $\theta_W = 19.2$ K for $\mu_0 H \perp c$ and $\theta_W = 41.9$ K for $\mu_0 H // c$ show a similar anisotropy, and suggest competing ferromagnetic and antiferromagnetic interactions. Density functional theory (DFT) calculations recapitulate the insulating behavior and predict *A*-type Eu magnetic order, in agreement with our observations. Overall, such results allow us to expand our knowledge in the chemical perspectives in the nature of magnetism in Eu-based Zintl compounds and its correlation to the electrical conductivity.

II. METHODS

Single crystals of $EuZn_2P_2$ were synthesized using elemental Eu (ingot, Yeemeida Technology Co., LTD 99.995%), Zn (shots, Sigma-Aldrich 99.99%), red P (Sigma-Aldrich 97+%), and Sn (shots, Sigma-Aldrich 99.99%). The elements were put in a 1:2:2:45 ratio and a total mass of 5 g was put in a Canfield crucible (size: 2 mL). Zn and Sn were placed in the crucible at atmospheric conditions, while Eu and P were added later in an Ar-filled glove box. The Canfield crucible was placed in a quartz ampoule with quartz wool below and above the crucible, evacuated, and sealed under 1.2×10^{-2} Torr of pressure. The evacuated ampoules were loaded in a box furnace at an angle of 45°. The temperature was ramped at a rate of 100 °C/h to $T = 500$ °C for 4 h. This step allowed for Sn flux to be in a liquid state. The furnace was then ramped from $T = 500$ °C to $T = 1150$ °C at a rate of 100 °C/h and held for 24 h. The furnace was then slowly cooled to $T = 850$ °C at a rate of 5 °C/h, then removed hot, inverted, and immediately centrifuged. Centrifugation took 2–3 min. Hexagonal platelike crystals of size 3 mm along the long direction were removed from the frit. These single crystals of $EuZn_2P_2$ were found to be stable in air over a period of months.

Powder x-ray diffraction (XRD) data, used to confirm phase purity of the single crystals, were collected over an angle range of 5 °–60° on a laboratory Bruker D8 Focus diffractometer with a LynxEye detector and Cu $K\alpha$ radiation. Single-crystal x-ray data were collected on a Bruker-Nonius X8 Proteum (Mo $K\alpha$ radiation) diffractometer equipped with an Oxford cryostream. Integration and scaling were performed using CRYSALISPRO (Version 1.171.39.29c, Rigaku

TABLE I. Crystal data and refinement results for $EuZn_2P_2$.

Formula	$EuZn_2P_2$
Crystal system	Trigonal
Space group	$P\bar{3}m1$ (No. 164)
FW (g/mol)	268.96
a (Å)	4.08497(18)
c (Å)	7.0019(4)
V (Å^3)	101.187(11)
Z	1
T (K)	213 (2)
Adsorption coefficient	27.612
Mo $K\alpha$ (Å)	0.71073
Reflections collected/number of parameters	180/10
Goodness of fit	1.188
R[F][a]	0.0104
$R_w(F_o^2)$[b]	0.0246

[a] $R(F) = \Sigma||F_o|-|F_c||/\Sigma|F_o|$.

[b] $R_w(F_o^2) = [\Sigma w(F_o^2 - F_c^2)^2 \Sigma w(F_o^2)^2]^{1/2}$.

OD, 2017). A multiscan absorption correction was applied using SADABS [19].The structure was solved by direct methods, and successive interpretations of difference Fourier maps were followed by least-squares refinement using SHELX and WINGX [20,21].

Magnetization data were collected on a Quantum Design magnetic property measurement system (MPMS). Magnetic susceptibility was approximated as magnetization divided by the applied magnetic field ($\chi \approx M/H$). To account for shape effects, a demagnetization correction was incorporated, with $N = 0.76$ for $\mu_0 H//c$ and $N = 0.18$ for $\mu_0 H \perp c$. In addition, heat capacity data were collected on a Quantum Design physical properties measurement system using the semiadiabatic method and a 1% temperature rise.

The resistivity measurements were performed in a Quantum Design physical property measurement system (PPMS) using a Lake Shore Model 372 AC resistance bridge. An AC current set to autorange between 10 nA and 1μA with an excitation frequency of 13.7 Hz was applied. The measurement was performed on a crystal with a four-probe configuration consisting of platinum wires and Epo-Tek silver epoxy H20E-FC. The picture of the single crystal with the Pt leads can be found in Fig. 6(a).

Density functional theory (DFT) based first principles calculations were performed using the projector augmented wave (PAW) method as implemented in the VASP code [22,23]. We used the PBE exchange-correlation functional as parametrized by Perdew-Burke-Ernzerhof [24,25]. For the self-consistent calculations a Monkhorst-Pack k mesh of size 15×15×5 was used to sample the Brillouin zone (BZ). The energy cutoff is chosen 1.5 times as large as the values recommended in relevant pseudopotentials. Spin-orbit coupling (SOC) was included self-consistently. The Eu $4f$ states were treated by employing the GGA $+U$ approach with the U value set to 5.0 eV. Our calculations do not consider the effect of spin-orbit coupling, which is expected to be too weak to significantly affect the band gaps and exchange couplings that are the focus of the present work. The Eu $4f$ electrons were treated differently in the nonmagnetic (NM) case, where we used a Eu pseudopotential with $4f$ electrons in the core.

III. RESULTS AND DISCUSSION

A. Structure

The single-crystal x-ray diffraction (SCXRD) data for $EuZn_2P_2$ at $T = 213$ K are consistent with the previously reported structure with the trigonal space group, P-3m1 [26]. A precession image along the (hk0) plane is shown in Fig. 1(a). Tables I–III provide the details, atomic coordinates, and atomic displacement parameters of the final refinement, which converged to $R1 = 1.04\%$ and $wR2 = 2.46\%$. The bond valence sum for Eu is 1.6+ implying that the Eu is divalent, i.e., Eu^{2+} [26]. As-grown crystals of $EuZn_2P_2$, Fig. 1(b), were found to be phase pure via powder x-ray diffraction after cleaning the excess tin from surfaces. The Zintl structure of $EuZn_2P_2$, Fig. 1(c), contains Eu^{2+} layers separated by an anionic framework of $[Zn_2P_2]^{2-}$ edge-sharing tetrahedra. The stacking of these layers forms an octahedral coordination environment for Eu^{2+}.

The structure of $EuZn_2P_2$ is a member of the La_2O_3 family, sometimes called the Ce_2O_2S type, and structurally written as $[La_2O_2]^{2+}O^{2-}$ [18,27]. $EuZn_2P_2$ is formally of the anti-La_2O_3 type (more commonly known as the $CaAl_2Si_2$ type), with anionic $[Zn_2P_2]^{2-}$ layers and cationic Eu^{2+}. Looking beyond those containing Eu, this is a very common structure type, including binaries such as Mg_3Sb_2 [Fig. 1(d)], ternaries such as Li_2MnO_2 [Fig. 1(e)], and quaternaries such as $NaLiCdS_2$ [Fig. 1(f)] [27–31]. All these structures crystallize into the same P-3m1 space group rationalized by the Zintl concept where the cations donate their valence electrons to stabilize the anionic tetrahedral framework. In these structures, individual tetrahedra are polar—with an elongation along the stacking axis (c axis), for example, in the case of $EuZn_2P_2$, one Zn-P bond being 2.5303(10) Å, but the three equivalent Zn-P bonds being 2.4608(3) Å. These units are arranged in an alternating up/down pattern so there is no net electric polarity even in a single layer. However, the anionic layers might be expected to have a significant electric quadrupolar response, something that is worthy of future study.

TABLE II. Fractional atomic coordinates and isotropic displacement parameters based on the refined $EuZn_2P_2$ structure.

Element	Wyckoff positions	x	y	z	Occupancy	U_{iso}
Eu	1a	1	1	0	1	0.00674(10)
Zn	2d	2/3	1/3	0.36947(6)	1	0.00791(11)
P	2d	1/3	2/3	0.26915(12)	1	0.00637(16)

TABLE III. Anistropic displacement parameters based on the refined $EuZn_2P_2$ structure.

Element	U_{11}	U_{22}	U_{33}	U_{23}	U_{13}	U_{12}
Eu	0.00656(11)	0.00656(11)	0.00711(13)	0.000	0.000	0.00328(5)
Zn	0.00781(13)	0.00781(13)	0.0081(2)	0.000	0.000	0.00391(6)
P	0.0061(2)	0.0061(2)	0.0068(4)	0.000	0.000	0.00307(11)

B. Heat capacity

As Eu magnetic order is expected, heat capacity measurements were carried out on $EuZn_2P_2$ single crystals from $T = 2$ to 300 K to identify possible phase transitions. A lambda anomaly at $T_N = 23$ K is observed, Fig. 2(a), and, when combined with magnetization (*vide infra*), is indicative of Eu antiferromagnetic order. The overall shape of the transition—a sharp peak followed by a broad hump at lower temperatures—is commonly observed in $S = 7/2$ magnets on simple-cubic-like lattices [31]. Extraction of the magnetic contribution to the specific heat is nontrivial, as the most direct nonmagnetic structural analog would be $BaZn_2P_2$, which adopts the distinct $ThCr_2Si_2$ structure type, whereas others have large differences in molar masses relative to $EuZn_2P_2$ [32]. We thus chose to construct a phonon model to fit the high temperature specific heat. The chosen model, the two-Debye model, is given by

$$\frac{C_p}{T} = \frac{C_{\rm D}(\theta_{\rm D1}, s_1, T)}{T} + \frac{C_{\rm D}(\theta_{\rm D2}, s_2, T)}{T}, \quad (1)$$

$$C_{\rm D}(\theta_{\rm D}, T) = 9sR\left(\frac{T}{\theta_{\rm D}}\right)^3 \int_0^{\theta_{\rm D}/T} \frac{(\theta/T)^4 e^{\theta/T}}{[e^{\theta/T} - 1]^2} d\frac{\theta}{T}, \quad (2)$$

where $\theta_{\rm D1}$ and $\theta_{\rm D2}$ are the Debye temperatures, s_1 and s_2 are the oscillator strengths, and R is the molar Boltzmann constant. When fitting phonons in heat capacity, we commonly fit using Debye and Einstein models which correspond to acoustic and optic phonons. In the $EuZn_2P_2$ single crystals, a single-Debye model was not sufficient to fit the experimental data. The Einstein model could not incorporate because there was no $T_{\rm max}$ in the C_p/T^3 versus T plot (not shown in the manuscript). Therefore, we tried a combination of two Debye models, which not only fitted the experimental data well but also gave physical oscillator terms that added up to the total number of atoms in the formula unit. The fit and physical oscillator terms made for criteria for our choice of two-Debye models. It is physically motivated by the distinct subunits: The phonon modes of the anion framework are expected to be distinct, energetically, from those arising from the cationic lattice, and are commonly observed in complex materials [14,32,33]. The model parameters from the least-squares refinement to the data for $T > 25$ K are given in Table IV. The total oscillator strength $s_1 + s_2 = 5.18(6)$. This is in good agreement with the expected value of $1 + 2 + 2 = 5$, the total number of atoms per formula unit in $EuZn_2P_2$.

After subtracting this phonon contribution, the sample heat capacity from $T = 2$ to 300 K was integrated to determine the change in entropy corresponding to magnetic order in $EuZn_2P_2$. Figure 2(b) shows that the change in the magnetic entropy reaches a maximum of $\Delta S_{\rm mag} = 11.3\ {\rm J\ mol^{-1}\ K^{-1}}$ just above T_N. A compound that consists of Eu^{2+} without any multivalence of Eu or other magnetic ions should have a recovery of entropy $\Delta S_{\rm mag} = R\ln(8) = 17.3\ {\rm J\ mol^{-1}\ K^{-1}}$, so the observed value is $\sim\frac{2}{3}$ of that expected. The most likely explanation is that the two-Debye model is overestimating

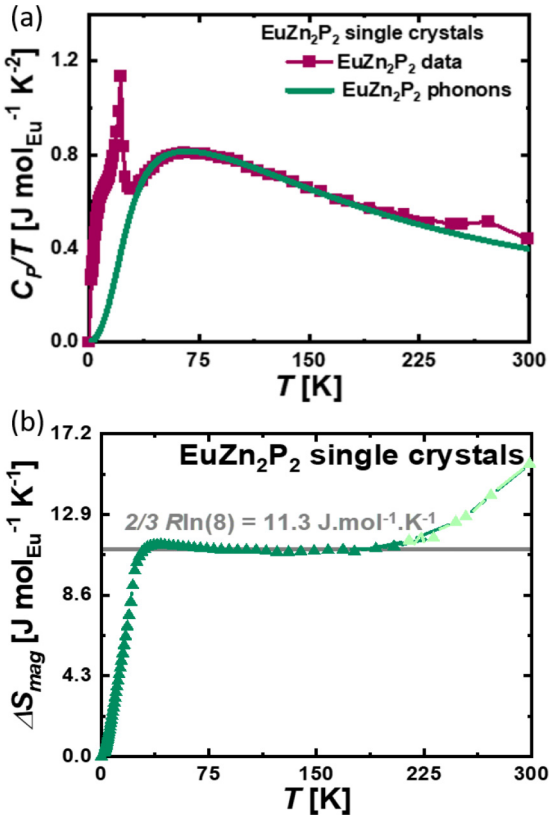

FIG. 2. (a) Specific heat divided by temperature as a function of temperature for $EuZn_2P_2$ single crystals from $T = 2$ to 300 K. The maroon-filled squares denote experimental data, and the green is the phonons modeled using the two-Debye model from $T = 30$–300 K. The sharp transition at $T = 25$ K is attributed to the antiferromagnetic phase transition. The bump around $T = 270$ K is from Apiezon N grease used during the measurement. (b) The change in magnetic entropy was integrated after subtracting the phonons from $T = 2$ to 300 K. The $\Delta S_{\rm mag}$ is close to $\sim \frac{2}{3}R\ln(8)$. The light green in $\Delta S_{\rm mag}$ at around $T = 270$ K is coming from Apiezon N grease.

TABLE IV. Fitting parameters to the C_p/T as a function of T for $EuZn_2P_2$ to extract the phonon contribution.

s_{D1} (Oscillator strength/formula unit)	s_{D2} (Oscillator strength/formula unit)	θ_{D1} (K)	θ_{D2} (K)
2.35(3)	2.83(3)	493(4)	182(3)

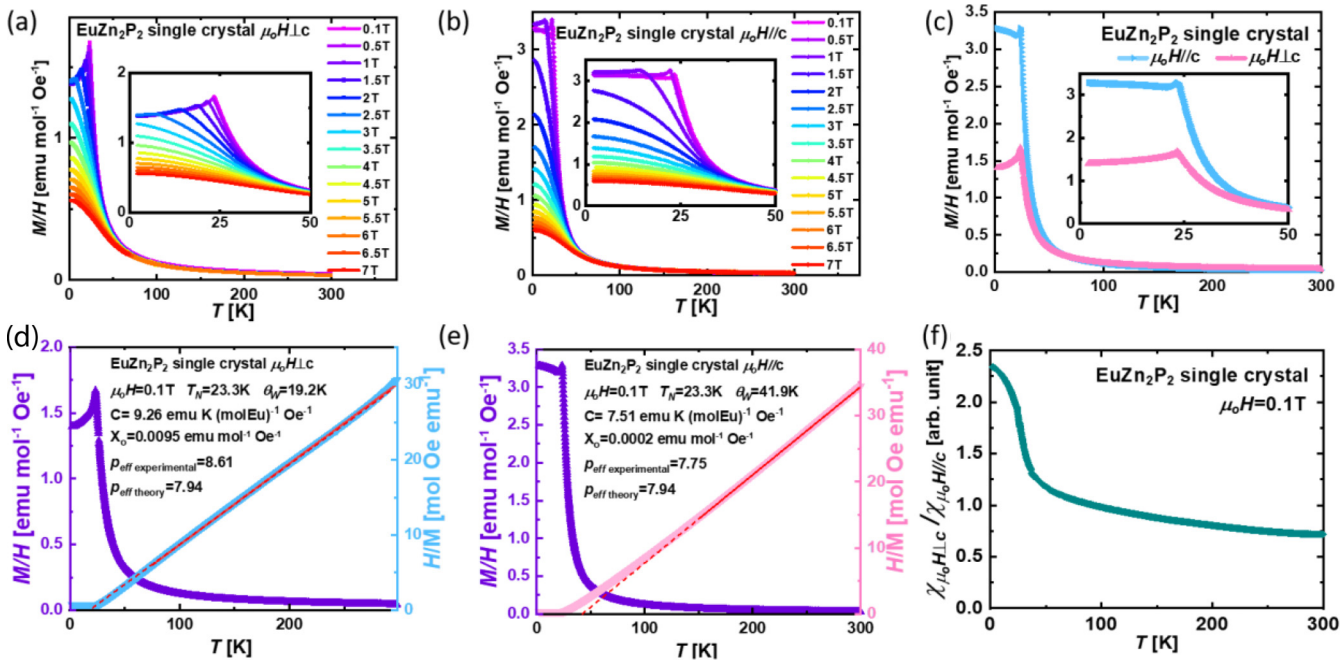

FIG. 3. (a) Magnetization as a function of temperature with $\mu_0 H||c$ and $\mu_0 H = 0.1$–7 T and $T = 2$–300 K. The $\mu_0 H = 0.1$ T data show a clear AFM transition at $T = 25$ K, with a decrease in both sharpness of the transition and the temperature of the transition as the field increases. (b) Magnetization as a function of temperature $\mu_0 H \perp c$ from $\mu_0 H = 0.1$ to 7 T and $T = 2$ to 300 K. The $\mu_0 H = 0.1$ T data show a kink at $T = 25$ K followed by an upturn, both of which are suppressed for $\mu_0 H > 0.1$ T. (c) Comparison in the magnetization as a function of temperature, $\mu_0 H \perp c$ and $\mu_0 H||c$, at $\mu_0 H = 0.1$ T over $T = 2$–300 K. (d) Curie Weiss analysis for $\mu_0 H||c$ from $\mu_0 H = 0.1$ T in the range $T = 2$–300 K, (e) Curie Weiss analysis $\mu_0 H \perp c$ from $\mu_0 H = 0.1$ and $T = 2$–300 K, and (f) ratio of magnetization $\mu_0 H||c$ and $\mu_0 H \perp c$ at $\mu_0 H = 0.1$ T and $T = 2$–300 K displaying the anisotropy below T_N.

the phonon contribution, particularly in the region just above T_N, as a gradual continued entropy recovery is expected for $S = 7/2$ beyond T_N [31]. We also attribute the factor of $\sim\frac{2}{3}$ to some magnetic fluctuations generated from the trigonal lattice, which is known in some cases to host a classical spin liquid [34]. The unphysical dip of the integrated ΔS_{mag} above T_N in Fig. 2(b) is consistent with this possibility. However, another possibility that cannot be ruled out is that there is additional entropy below $T = 2$ K that is not captured by a linear extrapolation of Cp/T approaching 0 at $T = 0$ K. One cannot completely rule out artifacts and the presence of magnetic entropy beyond the phonon subtraction region; thus the heat capacity analysis had some considerations and limitations.

C. Magnetization

Magnetization measurements provide details on the type of magnetic order in $EuZn_2P_2$ and enable determination of the magnetic phase diagram. Temperature-dependent magnetic susceptibility, measured with an applied field perpendicular and parallel to the layers (c axis), Figs. 3(a) and 3(b) show a clear antiferromagnetic phase transition at $T_N = 23$ K. The data from $T = 75$ to 300 K for $\mu_0 H \perp c$ and $T = 150$ to 300 K for $\mu_0 H//c$ are well described by the Curie-Weiss law:

$$\chi = \frac{C}{T - \theta_W} + \chi_0, \tag{3}$$

where χ_0 is the temperature-independent susceptibility, C is the Curie constant, and θ_W is the Weiss temperature. The fits are shown in Figs. 3(d) and 3(e) and the best least-squares parameters are given in Table V. The p_{eff} extracted from the Curie constants are 8.61 for $\mu_0 H \perp c$ and 7.75 for $\mu_0 H//c$, consistent with the theoretical $p_{\text{eff}} = 7.94$ for Eu^{2+}. The positive Weiss constants indicate dominant ferromagnetic interactions; in combination with the observed antiferromagnetic order, this implies a mixture of magnetic exchange interactions. Another noticeable feature in the susceptibility data is the anisotropy in $\mu_0 H \perp c$ and $\mu_0 H//c$, Figs. 3(c) and 3(f). The anisotropy is larger below the T_N in comparison to above the T_N with $\chi_\perp/\chi_{//}$ in the range 0.8–1.25 above T_N, rising rapidly below T_N to $\chi_\perp/\chi_{//} \sim 2.3$ at $T = 2$ K. This anisotropy is not due to demagnetization—which has been corrected for these data—and instead implies spin alignment in the ab plane below T_N. This is in agreement with observations on related Eu compounds [35–39].

To further evaluate the magnetic behavior, $M(H)$ curves were collected as a function of temperature for both $\mu_0 H \perp c$ and $\mu_0 H//c$, Figs. 4(a) and 4(b). In both crystal directions,

TABLE V. Fitting parameters obtained by Curie Weiss analysis from magnetization data of $EuZn_2P_2$.

$EuZn_2P_2$	$\mu_0 H \perp c$	$\mu_0 H \parallel c$
Range (K)	150–300	150–300
C [emu K (mol Eu)$^{-1}$ Oe^{-1}]	9.26	7.51
θ (K)	19.2	41.9
χ_0 [emu^{-1} (mol Eu) Oe]	0.0095	0.0002
p_{eff}	8.61	7.75

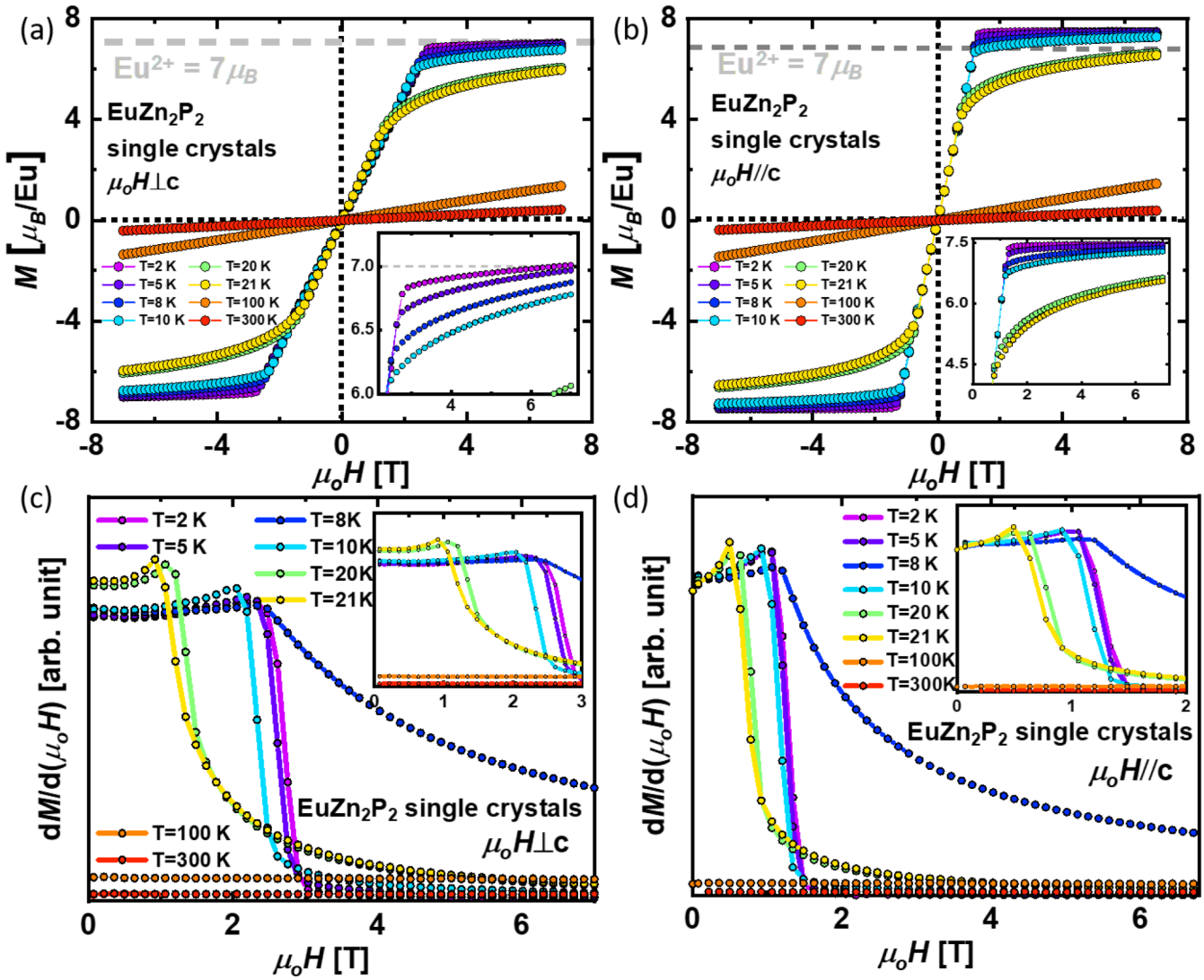

FIG. 4. For each plot, the following temperatures are shown: $T = 2$, 5, 8, 10, 20, 21, 100, and 300 K. (a) Magnetization as a function of magnetic field with $\mu_0 H||c$ from $\mu_0 H = -7$ to 7 T; (b) magnetization as a function of magnetic field with $\mu_0 H \perp c$ from $\mu_0 H = -7$ to 7, (c) derivative of magnetization over magnetic field as a function of magnetic field with $\mu_0 H||c$, and (d) derivative of magnetization over magnetic field as a function of magnetic field with $\mu_0 H \perp c$.

the magnetization saturates at $7\,\mu_B$, the expected value for divalent Eu^{2+}. This saturation rules out any Eu^{2+}/Eu^{3+} mixed valency in $EuZn_2P_2$. The highly linear $M(H)$ behavior before saturation in both directions is common to many Eu^{2+} materials [36–39]. However, there are noticeable differences in the $M(H)$ data in the $\mu_0 H \perp c$ and $\mu_0 H//c$ directions. The saturation of $7\mu_B$ happens at different magnetic fields, which implies that there is a difference in the magnetic stiffness in the two directions. These anisotropic features are consistent with the susceptibility results in Figs. 3(a)–3(f). It takes little applied magnetic field ($\mu_0 H = 0.75$ T) to fully polarize the spins in the $\mu_0 H//c$ direction in comparison to the $\mu_0 H \perp c$ direction ($\mu_0 H = 2.25$ T). This behavior implies a higher anisotropy in plane than out of plane and no signs of spin glass behavior. The θ_W is usually attributed to ferromagnetic interactions. However, from $M(T)$ we observe that the overall magnetic order is most definitely antiferromagnetic (the sharp peak is attributed to T_N). However, if we look at individual Eu layers, it is apparent that the Eu atoms within a plane are ferromagnetically coupled to one another (i.e., the intralayer interaction is ferromagnetic), whereas each layer is antiferromagnetically coupled to adjacent layers (i.e., the interlayer interaction is antiferromagnetic). The positive θ_W is indicative of dominance of ferromagnetic interactions (coming from intralayer interactions which are ferromagnetic layers) over the antiferromagnetic layers (interlayer interactions). Another feature is that the Eu spins in the $EuZn_2P_2$ do not undergo any apparent phase transitions as a function of field and smoothly transition into the field-polarized state. To extract the characteristic fields associated with these behaviors, Figs. 4(c) and 4(d) show the derivative as a function of the field.

Figures 5(a) and 5(b) show the critical fields in $M(H)$ as a function of field direction. From the $M(T)$ measurements in Figs. 3(a) and 3(b), we know that $EuZn_2P_2$ is net antiferromagnetic. The Eu spins then reorient themselves to a field-polarized paramagnetic/ferromagnetic state on applying

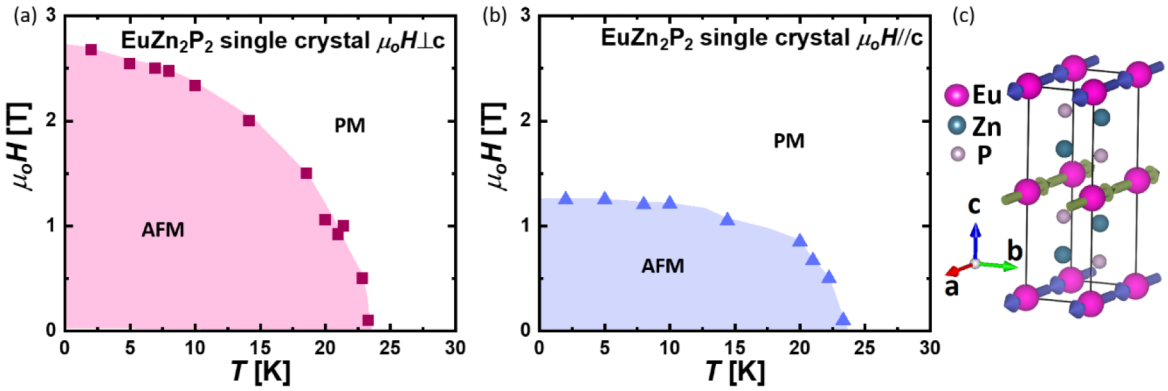

FIG. 5. Magnetic phase diagram of $EuZn_2P_2$ with (a) $\mu_0 H \perp c$ and (b) $\mu_0 H || c$. In both cases, there is an anisotropic AFM state at low fields, followed by a PM state that continuously evolves to a field-polarized state. The transition from AFM to a field-polarized state was determined from the maximum in the $M(T)$ data. (c) Proposed A-type antiferromagnetic structure of $EuZn_2P_2$.

a sufficiently large magnetic field. These data are sufficient to identify the type of magnetic order present: As described above, the spins lie in the ab plane. The order cannot be G type (all antiferromagnetic within and between Eu layers), since in that case a proper phase transition should be observed with an applied field. The triangular lattice within each layer makes C-type order (ferromagnetic between layers, antiferromagnetic within layers) unlikely as there is no evidence of a structural phase transition. Further, with C-type order one would expect a field-driven magnetic transition along one of the two directions, while none are observed. We are thus left with A-type order (ferromagnetic layers stacked antiferromagnetically) as the prime candidate for the magnetic order. Such an order can continuously rotate to a field-polarized state independent of the applied field direction, in agreement with the data here. It is also in agreement with the known magnetic order in isostructural analogs [40–43].

D. Resistivity

To explore the electronic behavior, the temperature dependence of the electrical resistivity was measured for $T =$ 140–400 K, Fig. 6(a). The resistivity decreases with temperature in the paramagnetic state and the order of magnitude of the resistivity is $10^3\,\Omega\,\mathrm{cm}$ at $T = 300\,\mathrm{K}$ consistent with insulating behavior in $EuZn_2P_2$. In order to extrapolate the band gap through the resistance, the Arrhenius model was fitted to the resistivity data as $\ln(\rho/\rho_{T=400\,\mathrm{K}})$ versus T^{-1} in Fig. 6(b). In the Arrhenius model, a linear trend explains that the resistivity follows an activation-type relation, $\rho \propto e^{E_g/k_B T}$, and fits $EuZn_2P_2$ well over the range measured. The extracted band gap is $E_g = 0.11\,\mathrm{eV}$. We note that a recent conference proceedings claims to have observed similar behavior in $EuZn_2P_2$ [44].

E. Theory

DFT calculations were performed for all four simple magnetic configurations with spins in the ab plane: G-type, C-type, A-type, and all ferromagnetic (FM). The energies of FM, G-type AFM, and C-type AFM orders are found to be 1.75, 11.47, and 10.43 meV higher than the A-type AFM, which is lowest in energy, with the FM as a close second. Since G-type and C-type orders are much higher in energy, we did not include them in our considerations. The theory is thus in agreement with the magnetization measurements and provides further evidence of A-type order in $EuZn_2P_2$. In this case, the computed moments are $\pm 6.935\mu_\beta$ for the

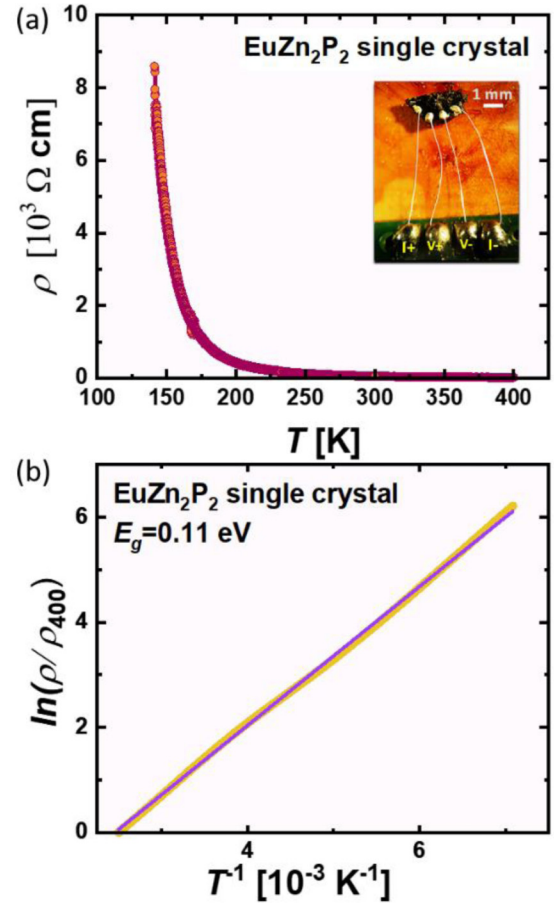

FIG. 6. (a) Four probe resistivity data of $EuZn_2P_2$ single crystals at $T =$ 140–400 K. (b) Natural logarithm of normalized resistivity as a function of $\frac{1}{T}$ measured on a single crystal of $EuZn_2P_2$ along the c axis. The band gap extrapolated is $E_g = 0.11\,\mathrm{eV}$ and is fit to $\ln(\frac{\rho}{\rho_{T=400\,\mathrm{K}}}) = \frac{E_g}{k_B}\frac{1}{T}$.

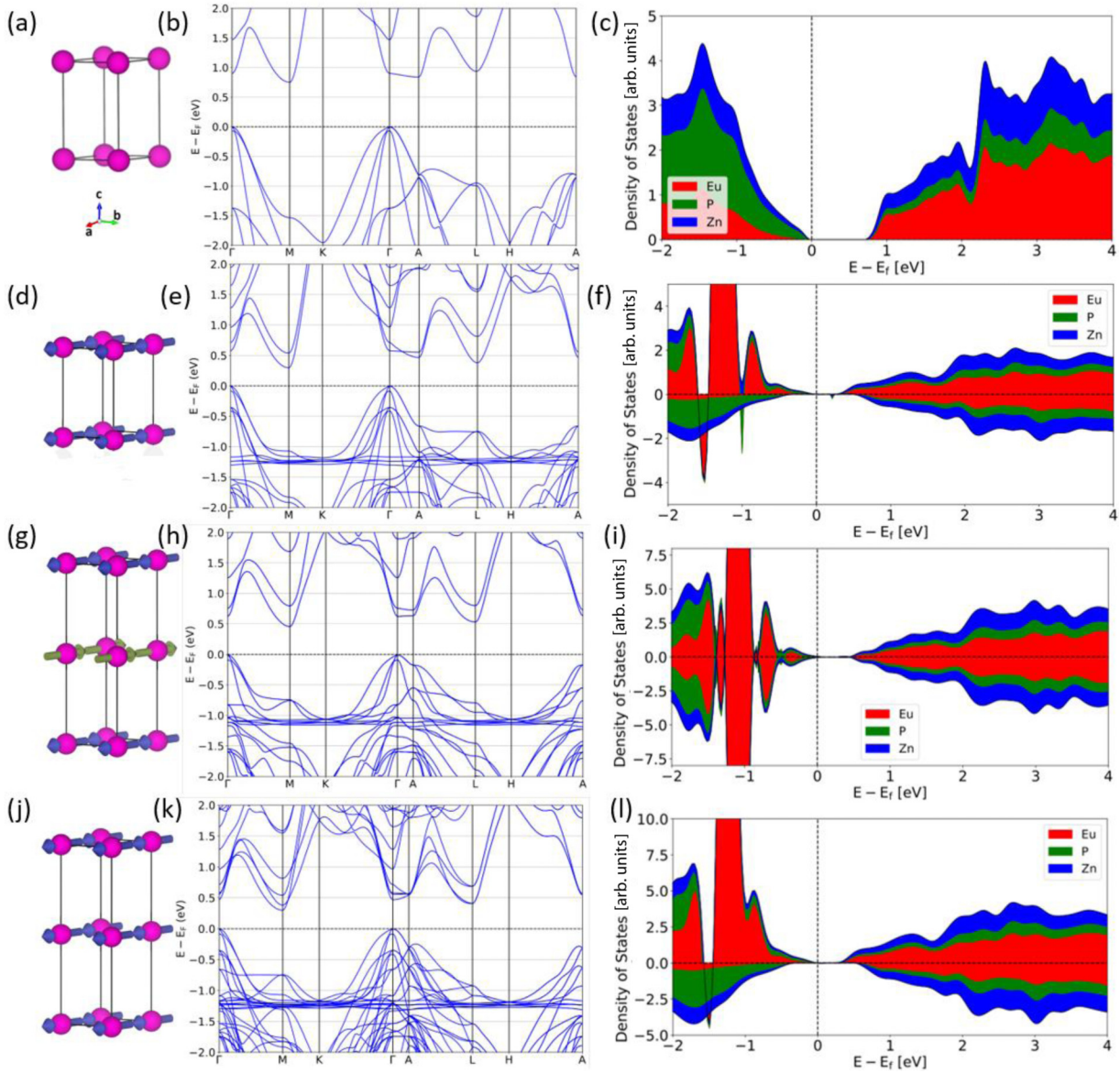

FIG. 7. Density functional theory (DFT) calculation in the nonmagnetic configuration (a)–(c), ferromagnetic configuration (single unit cell) (d)–(f), *A*-type antiferromagnetic configuration (g)–(i), and ferromagnetic configuration (doubled unit cell) (j)–(l). For each case we present the unit cell, band structure, and the density of states.

Eu, $\pm 0.005\mu_\beta$ for Zn, and $\pm 0.018\mu_\beta$ for the P, with no net moment on the Zn_2P_2 tetrahedra. DFT also predicts $EuZn_2P_2$ to be an electrical insulator in the antiferromagnetic state. This insulating behavior persists in the FM configuration, Fig. 7(b), and implies that $EuZn_2P_2$ should be an insulator at all temperatures, in agreement with experiment (we note that the gap for comparison to theory is $2E_g$ as defined here, i.e., 0.22 eV). The computed magnetic moments do change slightly in the FM case, becoming $6.930\mu_\beta$ for the Eu, $-0.007\mu_\beta$ for Zn, and $-0.027\mu_\beta$ for the P, with a total moment on the tetrahedra of $-0.066\mu_\beta$.

These calculations also demonstrate how the distinct subunits of a Zintl phase couple: The direct band gap at Γ is $E_g = 0.60$ eV in the antiferromagnetic configuration and $E_g = 0.48$ eV in the ferromagnetic configuration (a 20% change), and the indirect band gap from Γ to *M* is $E_g = 0.48$ eV in the antiferromagnetic configuration and $E_g = 0.30$ eV in the ferromagnetic configuration (a 38% change). The large change in activation energy occurs even though the states at the top of the valence band and the bottom of the conduction band are derived from the nonmagnetic Zn and P atoms (and not Eu)—Eu $4f$ states are 1.2 eV below the valence band maximum in both cases. Figure 8 and Table VI describe the shift in the

TABLE VI. Band gap extrapolated from *U* considerations at 4, 5, and 6 eV on the *A*-type AFM and FM cases corresponding to Fig. 8.

U (eV)	*A*-type AFM energy gap (eV)	FM energy gap (eV)
4	0.3692	0.1904
5	0.4685	0.3027
6	0.5359	0.3901

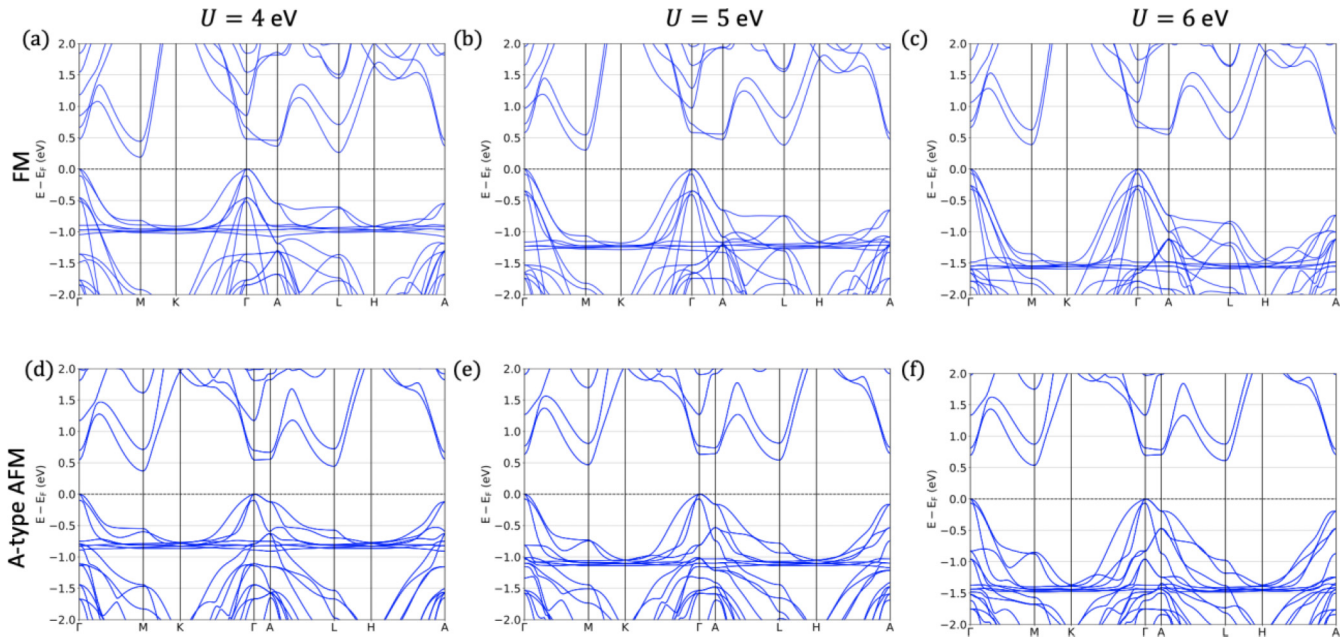

FIG. 8. Density functional theory (DFT) band structure for the (a)–(c) FM and the (d)–(f) A-type AFM cases for $U = 4, 5, 6$ eV. The plots show sensitivity of activation energy with the value of U.

activation energy as a function of U. While it is possible that the observed resistivity changes may arise from defect levels in the charge gap, they are also qualitatively consistent with the changes of gap seen in the DFT calculations

Given the impact of the Eu magnetism on the electronic structure of the Zn_2P_2 framework, it is natural to ask if the reverse is true—does the electronic structure of the anion framework significantly impact the magnetic order of the Eu lattice? To address this question, Table VII gives key parameters for a set of isostructural EuM_2X_2 (M = metal, X = pnictide) magnets, including intra- and interlayer distances, and room temperature resistivities. Note that in all cases, an insulating band structure (with either a positive or negative—i.e., semimetal—gap) is expected on the basis of electron count and bonding. Several trends are immediately apparent. First, $EuZn_2P_2$ has a higher Eu ordering temperature than any other known member of this family. Second, for a given metal M, the materials become more conductive and have a lower Eu ordering temperature as X increases down the pnictogen column. The magnitudes of the changes, however, are not uniform for different M. Given the large $J = S = 7/2$ for Eu^{2+}, if the Eu-Eu interactions are primarily dipolar in nature, then one expects the magnetic interaction strength, and hence T_N, to scale as $1/d^3$, where d is the interion separation. We note that this holds even if the M_2X_2 layers screen or enhance a portion of the dipolar interaction, as would be expected in general when the magnetic permeability is not exactly unity [52]. Simply using the intralayer or interlayer distances combined with number of nearest neighbors gives partial trends, but does not unify the observations across different choices of M. We thus applied a multilinear regression to determine if some linear combination of $1/d_{nn}^3$ (d_{nn} = intralayer Eu-Eu distance) and $1/d_{il}^3$ (d_{il} = interlayer Eu-Eu distance) could explain all the data in Table VII. This yielded coefficients close to a 1:–4 ratio. Fixing the combination at exactly this ratio yields the trend in Fig. 9, which shows a monotonic

TABLE VII. Key Eu lattice geometric parameters, observed magnetic ordering temperature, and room temperature resistivity, for a range of known EuM_2X_2 trigonal Zintl materials.

EuM_2X_2	Interlayer Eu-Eu distance (Å)	Intralayer Eu-Eu distance (Å)	Eu T_N (K)	ρ_{ab} (mΩ cm at $T = 300$ K)	References
$EuZn_2P_2$	7.0019	4.0845	23	66	This work
$EuZn_2As_2$	7.1810	4.2110	19	75	[26,40]
$EuZn_2Sb_2$	7.6090	4.4938	12	1.3	[41,42]
$EuMn_2P_2$	6.9936	4.1294	17	3.50×10^5	[45]
$EuMn_2As_2$	7.2250	4.2870	15	200	[36]
$EuMn_2Sb_2$	7.6740	4.5810	9.4	–	[36,37]
$EuCd_2P_2$	7.1790	4.3250	11	24	[46,47]
$EuCd_2As_2$	7.3500	4.4499	9.5	15	[48,49]
$EuCd_2Sb_2$	7.7230	4.6980	7.8	12	[47,50]
$EuMg_2Sb_2$	7.7240	4.6950	8.2	–	[51]
$EuMg_2Bi_2$	7.8483	4.7724	6.7	2.3	[38,39]

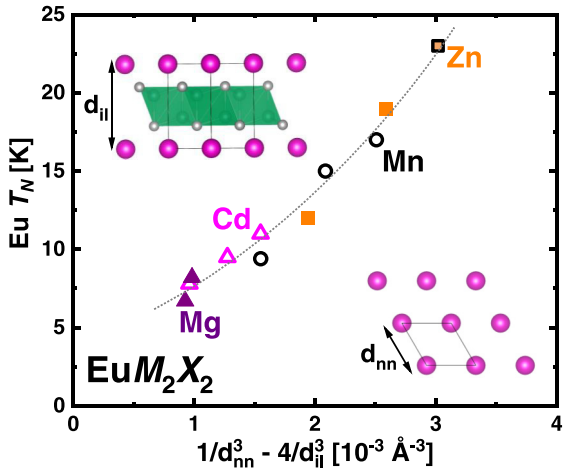

FIG. 9. The Eu magnetic ordering temperature of EuM_2X_2 materials scales with the inverse cubed distance between intralayer and interlayer Eu-Eu ions within the cationic lattice implying dominate dipolar interactions.

dependence of T_N on this mixture of Eu-Eu distances across different choices of M. This relationship holds across five orders of magnitude of conductivity, and demonstrates a dipolarlike scaling of the Eu-Eu interactions and suggests that the primary effect of the anionic framework is to modulate a dipolar interaction via changes in Eu-Eu distances (rather than, e.g., being due to superexchange or RKKY interactions which should be weak, and would not scale as $1/d^3$) [53]. The observed ratio of 1:–4 is also consistent with the structure. The full expression for the magnetic dipolar interaction energy is $= -\frac{\mu_0}{4\pi r^3}[3(m_1 \cdot \hat{r})(m_2 \cdot \hat{r}) - m_1 \cdot m_2]$. Depending on the orientation of the dipole moments (m_1, m_2) relative to the vector connecting the two dipolar sites ($\hat{r}$), the interaction can favor either ferromagnetic (when they are coparallel) or antiferromagnetic (when they are perpendicular) alignments. Thus, the sign of a dipolar magnetic interaction can be either positive or negative. From the observed order—in-plane ferromagnetic layers aligned antiferromagnetically—we expect the nearest neighbor interaction and the between-layer interaction to be opposite in sign, in agreement with the model (1 and −4). The magnitude of the coefficients, however, cannot just be extracted from the number (and relative distances) of nearest neighbors, because it also depends on the local magnetic permeability within, versus between, Eu layers, and also must account for (in an effective fashion) the longer range dipolar interactions—the next nearest neighbor in-plane interactions are about the same distance as the interlayer Eu-Eu ions for example. Further studies are necessary to determine whether this dipolarlike scaling arises from true dipolar interactions or other interactions manifesting in net as dipolar.

IV. CONCLUSION

$EuZn_2P_2$ single crystals prepared via a flux technique crystallize in the trigonal anti-La_2O_3 ($CaAl_2Si_2$) structure type and exhibit Eu antiferromagnetic order at $T_N = 23$ K. Heat capacity results showed a change in the magnetic entropy saturation at $\sim \frac{2}{3}R\ln(8)$ likely limited by the available phonon contribution model. Via magnetic susceptibility measurements the anisotropy of the $\mu_0 H \perp c$ and $\mu_0 H // c$ directions of $EuZn_2P_2$ single crystals was characterized. A significant anisotropy develops below T_N. The magnetic phase diagram allows identification of the magnetic structure of $EuZn_2P_2$ as A-type magnetic order. Resistivity measurements indicate insulating behavior with an experimental band gap of $E_g = 0.11$ eV, consistent with DFT calculations. Comparisons among related materials show that the dominant effect of the anionic framework on the Eu lattice magnetism scales as expected for magnetic dipolar interactions. Overall, our results help us gain insight into the polyanionic contributions to the conductivity and magnetism in the EuM_2X_2 structures. For future work, local probes to understand the local coordination environment in $EuZn_2P_2$ would allow understanding of the structural coordination and high resistance measurements would allow understanding of the conductivity close to Néel temperature to evaluate the conduction pathways in $EuZn_2P_2$.

ACKNOWLEDGMENTS

The authors would like to thank M. Siegler for technical assistance. This work was supported as part of the Institute for Quantum Matter and Energy Frontier Research Center, funded by the U.S. Department of Energy, Office of Science, Office of Basic Energy Sciences, under Award No. DE-SC0019331. The MPMS was funded by the National Science Foundation, Division of Materials Research, Major Research Instrumentation Program, under Award No. 1828490.

[1] Y. Xu, Z. Song, Z. Wang, H. Weng, and X. Dai, Higher-Order Topology of the Axion Insulator $EuIn_2As_2$, Phys. Rev. Lett. **122**, 256402 (2019).

[2] P. Rosa, Y. Xu, M. Rahn, J. Souza, S. Kushwaha, L. Veiga, A. Bombardi, S. Thomas, M. Janoschek, E. Bauer, M. Chan, Z. Wang, J. Thompson, N. Harrison, P. Pagliuso, A. Bernevig, and F. Ronning, Colossal magnetoresistance in a nonsymmorphic antiferromagnetic insulator, npj Quantum Mater. **5**, 52 (2020).

[3] L. Z. Sun, A. F. Wang, H. M. Mu, H. H. Wang, Z. F. Wang, T. Wu, Z. Y. Wang, X. Y. Zhou, and X. H. Chen, Field-induced metal-to-insulator transition and colossal anisotropic magnetoresistance in a nearly Dirac material $EuMnSb_2$, npj Quantum Mater. **6**, 1 (2021).

[4] J. Yan, Z. Z. Jiang, R. C. Xiao, W. J. Lu, W. H. Song, X. B. Zhu, X. Luo, Y. P. Sun, and M. Yamashita, Field-induced topological Hall effect in antiferromagnetic axion insulator candidate $EuIn_2As_2$, Phys. Rev. Research **4**, 013163 (2022).

[5] J. Shuai, J. Mao, S. Song, Q. Zhang, G. Chen, and Z. Rena, Recent progress and future challenges on thermoelectric Zintl materials, Mater. Today Phys. **1**, 74 (2017).

[6] N. Varnava, T. Berry, T. M. McQueen, and D. Vanderbilt, Engineering magnetic topological insulators in $Eu_5M_2X_6$ Zintls, arXiv:2203.06212.

[7] C. Chen, W. Xue, S. Li, Z. Zhang, X. Li, X. Wang, Y. Liu, J. Sui, X. Liu, F. Cao, Z. Ren, C.-W. Chu, Y. Wang, and Q. Zhang, Zintl-phase Eu_2ZnSb_2: A promising thermoelectric material with ultralow thermal conductivity, Proc. Natl Acad. Sci. USA **116**, 2831 (2019).

[8] T. F. Fässler and C. Kronseder, BaSn: A superconductor at the border of Zintl phases and intermetallic Compounds. Real-space analysis of band structures, Angew. Chem. Int. Ed. Engl. **36**, 2683 (1997).

[9] K. L. Hodge and J. E. Goldberger, Transition metal-free alkyne hydrogenation catalysis with $BaGa_2$, a hydrogen absorbing layered Zintl phase, J. Am. Chem. Soc. **141**, 19969 (2019).

[10] Z. Zada, A. Laref, G. Murtaza, A. Zeb, and A. Yar, First-principles calculations of electronic and magnetic properties of XMn_2y_2 (X = Ca, Sr; Y = Sb, Bi) compounds, Int. J. Mod. Phys. B **33**, 1950199 (2019).

[11] Z. Zada, H. Ullah, R. Zada, S. Laref, A. Azam, S. Khan, and A. A. Irfan, Structure stability, half metallic ferromagnetism, magneto-electronic and thermoelectric properties of new Zintl XCr_2Bi_2 (X = Ca, Sr) compounds for spintronic and renewable energy applications, Physica B **607**, 412866 (2021).

[12] A. Khan and A. H. Reshak, Optoelectronic and transport properties of Zintl phase KBa_2Cd_2Sb compound, Comput. Mater. Sci. **95**, 328 (2014).

[13] M. Kumar, N. Umezawa, W. Zhou, and M. Imai, Electronic states of Zintl-phase solar-cell material $BaSi_2$, J. Mater. Chem. A **5**, 25293 (2017).

[14] T. Berry, S. R. Parkin, and T. M. M. McQueen, Antiferro-and metamagnetism in the $S = 7/2$ hollandite analog $EuGa_2Sb_2$, Phys. Rev. Materials **5**, 114401 (2021) .

[15] K. P. Devlin, J. Zhang, J. C. Fettinger, E. S. Choi, A. K. Hauble, V. Taufour, R. P. Hermann, and S. M. Kauzlarich, Deconvoluting the magnetic structure of the commensurately modulated quinary Zintl phase $Eu_{11-x}Sr_xZn_4Sn_2As_{12}$, Inorg. Chem. **60**, 5711 (2021).

[16] D. Zhang, M. Shi, T. Zhu, D. Xing, H. Zhang, and J. Wang, Topological Axion States in Magnetic Insulator $MnBi_2Te_4$ with the Quantized Magnetoelectric Effect, Phys. Rev. Lett. **122**, 206401 (2019).

[17] S. Bobev, E. D. Bauer, J. D. Thompson, J. L. Sarrao, G. J. Miller, B. Eck, and R. Dronskowski, Metallic behavior of the Zintl phase $EuGe_2$: Combined structural studies, property measurements, and electronic structure calculations, J. Solid State Chem. **177**, 3545 (2004).

[18] C. Zheng, R. Hoffmann, R. Nesper, and H. G. Von Schnering, Site preferences and bond length differences in $CaAl_2Si_2$-type Zintl compounds, J. Am. Chem. Soc. **108**, 1876 (1986).

[19] R. C. Clark and J. S. Reid, The analytical calculation of absorption in multifaceted crystals, Acta Cryst. A **51**, 887 (1995).

[20] G. A. Sheldrick, Short history of SHELX, Acta Cryst. A **64**, 112 (2008).

[21] G. A. Sheldrick, SHELXT-integrated space-group and crystal-structure determination, Acta Cryst. A **71**, 3 (2015).

[22] P. Hohenberg and W. Kohn, Inhomogeneous electron gas, Phys. Rev. **136**, B864 (1964).

[23] W. Kohn and L. J. Sham, Self-consistent equations including exchange and correlation effects, Phys. Rev. **140**, A1133 (1965).

[24] G. Kresse and J. Furthmuller, Efficient iterative schemes for *ab initio* total-energy calculations using a plane-wave basis set, Phys. Rev. B **54**, 11169 (1996).

[25] G. Kresse and D. Joubert, From ultrasoft pseudopotentials to the projector augmented-wave method, Phys. Rev. B **59**, 1758 (1999).

[26] P. Klüfers, H. Neumann, A. Mewis, and H. Schuster, AB_2X_2-Verbindungen im $CaAl_2Si_2$-Typ, VIII [1]/AB_2X_2 compounds with the $CaAl_2Si_2$ structure, VIII [1], Z. Naturforsch. B **35**, 1317 (1980).

[27] W. C. Koehler and E. O. Wollan, Neutron-diffraction study of the structure of the A-form of the rare earth sesquioxides, Acta Cryst. **6**, 741 (1953).

[28] J. Zhang, L. Song, and B. B. Iversen, Insights into the design of thermoelectric Mg_3Sb_2 and its analogs by combining theory and experiment, npj Comput. Mater. **5**, 76 (2019).

[29] W. I. F. David, J. B. Goodenough, M. M. Thackeray, and M. G. S. R. Thomas, The crystal structure of Li_2MnO_2, Rev. Chim. Miner. **20**, 636 (1983).

[30] B. Deng, G. H. Chan, F. Q. Huang, D. L. Gray, D. E. Ellis, R. P. Van Duyne, and J. A. Ibers, Synthesis, structure, optical properties, and electronic structure of $NaLiCdS_2$, J. Solid State Chem. **180**, 759 (2007).

[31] R. Lora-Serrano, D. J. Garcia, D. Betancourth, R. P. Amaral, N. S. Camilo, E. Estévez-Rams, L. A. Ortellado G. Z., and P. G. Pagliuso, Dilution effects in spin 7/2 systems. The case of the antiferromagnet $GdRhIn_5$, J. Magn. Magn. Mater. **405**, 304 (2016).

[32] T. Berry, L. A. Pressley, W. A. Phelan, T. T. Tran, and T. M. McQueen, Laser-enhanced single crystal growth of non-symmorphic materials: Applications to an eight-fold fermion candidate, Chem. Mater. **32**, 5827 (2020).

[33] M. Sinha, H. K. Vivanco, C. Wan, M. A. Siegler, V. J. Stewart, E. A. Pogue, L. A. Pressley, T. Berry, Z. Wang, J. I. Johnson, M. Chen, T. T. Tran, W. A. Phelan, and T. M. McQueen, Twisting of 2D kagomé sheets in layered intermetallics, ACS Cent. Sci. **7**, 1381 (2021).

[34] Z. Zhu, P. A. Maksimov, S. R. White, and A. L. Chernyshev, Topography of Spin Liquids on a Triangular Lattice, Phys. Rev. Lett. **120**, 207203 (2018).

[35] A. Balvanz, S. Baranets, M. O. Ogunbunmi, and S. Bobev, Two polymorphs of $BaZn_2P_2$: Crystal structures, phase transition, and transport properties, Inorg. Chem. **60**, 14426 (2021).

[36] V. K. Anand and D. C. Johnston, Metallic behavior induced by potassium doping of the trigonal antiferromagnetic insulator $EuMn_2As_2$, Phys. Rev. B **94**, 014431 (2016).

[37] R. Rühl and W. Jeitschko, New pnictides with Ce_2O_2 S-type structure, Mater. Res. Bull. **14**, 513 (1979).

[38] A. F. May, M. A. McGuire, D. J. Singh, R. Custelcean, and G. E. Jellison, Structure and properties of single crystalline $CaMg_2Bi_2$, $EuMg_2Bi_2$, and $YbMg_2Bi_2$, Inorg. Chem. **50**, 11127 (2011).

[39] S. Pakhira, M. A. Tanatar, and D. C. Johnston, Magnetic, thermal, and electronic-transport properties of $EuMg_2Bi_2$ single crystals, Phys. Rev. B **101**, 214407 (2020).

[40] J. Blawat, M. Marshall, J. Singleton, E. Feng, H. Cao, W. Xie, and R. Jin, Unusual electrical and magnetic properties in layered $EuZn_2As_2$, Adv. Quantum Technol. **5**, 2200012 (2022).

[41] A. F. May, M. A. Guire, J. Ma, O. Delaire, A. Huq, and R. Custelcean, Properties of single crystalline AZn_2Sb_2 (A = Ca, Eu, Yb), J. Appl. Phys. **111**, 033708 (2012).

[42] I. Schellenberg, M. Eul, W. Hermes, and R. A. Pöttgen, ^{121}Sb and ^{151}Eu Mössbauer spectroscopic investigation of $EuMn_2Sb_2$, $EuZn_2Sb_2$, $YbMn_2Sb_2$, and $YbZn_2Sb_2$, Z. Anorg. Allg. Chem. **636**, 85 (2010).

[43] A. C. Payne, A. E. Sprauve, M. M. Olmstead, S. M. Kauzlarich, J. Y. Chan, B. A. Reisner, and J. W. Lynn, Synthesis, magnetic and electronic properties of single crystals of $EuMn_2P_2$, J. Solid State Chem. **163**, 498 (2002).

[44] Z. Bukowski, Magnetism, superconductivity and magnetotransport properties of Eu-based ternary pnictides, Pedagogical University of Cracow, 2021.

[45] T. Berry *et al.* (private communication).

[46] Z. C. Wang, J. D. Rogers, X. Yao, R. Nichols, K. Atay, B. Xu, J. Franklin, I. Sochnikov, P. J. Ryan, D. Haskel, and F. Tafti, Colossal magnetoresistance without mixed valence in a layered phosphide crystal, Adv. Mater. **33**, 2005755 (2021).

[47] A. Artmann, A. Mewis, M. Roepke, and G. Michels, AM_2X_2-Verbindungen mit $CaAl_2Si_2$ struktur. XI. Struktur und eigenschaften der verbindungen ACd_2X_2 (A: Eu, Yb; X: P, As, Sb), Z. Anorg. Allg. Chem. **622**, 679 (1996).

[48] J.-Z. Ma, S. M. Nie, C. J. Yi, J. Jandke, T. Shang, M. Y. Yao, M. Naamneh, L. Q. Yan, Y. Sun, A. Chikina, V. N. Strocov, M. Medarde, M. Song, Y.-M. Xiong, G. Xu, W. Wulfhekel, J. Mesot, M. Reticcioli, C. Franchini, C. Mudry *et al.*, Spin fluctuation induced Weyl semimetal state in the paramagnetic phase of $EuCd_2As_2$, Sci. Adv. **5**, eaaw4718 (2019).

[49] I. Schellenberg, U. Pfannenschmidt, M. Eul, C. Schwickert, and A R. Pöttgen, ^{121}Sb and ^{151}Eu Mössbauer spectroscopic investigation of $EuCd_2X_2$ (X = P, As, Sb) and $YbCd_2Sb_2$, Z. Anorg. Allg. Chem. **637**, 1863 (2011).

[50] H. Su, B. Gong, W. Shi, H. Yang, H. Wang, W. Xia, Z. Yu, P.-J. Guo, J. Wang, L. Ding, L. Xu, X. Li, X. Wang, Z. Zou, N. Yu, Z. Zhu, Y. Chen, Z. Liu, K. Liu, and G. Li, Magnetic exchange induced Weyl state in a semimetal $EuCd_2Sb_2$, APL Mater. **8**, 011109 (2020).

[51] F. Wartenberg, C. Kranenberg, R. Pocha, D. Johrendt, A. Mewis, R. D. Hoffmann, B. D. Mosel, and R. Pottgen, New pnictides with the $CaAl_2Si_2$ type structure and the stability range of this type, Z. Naturforsch., B **57**, 1270 (2002).

[52] P. Hammond, *Electric and Magnetic Images*, IEE Monograph No. 379 (Institution of Electrical Engineers, New York 1960).

[53] D. C. Johnston, Magnetic dipole interactions in crystals, Phys. Rev. B **93**, 014421 (2016).